Volume 16
Number 20
28 May 2025
Pages 8597–9032

Chemical Science

rsc.li/chemical-science

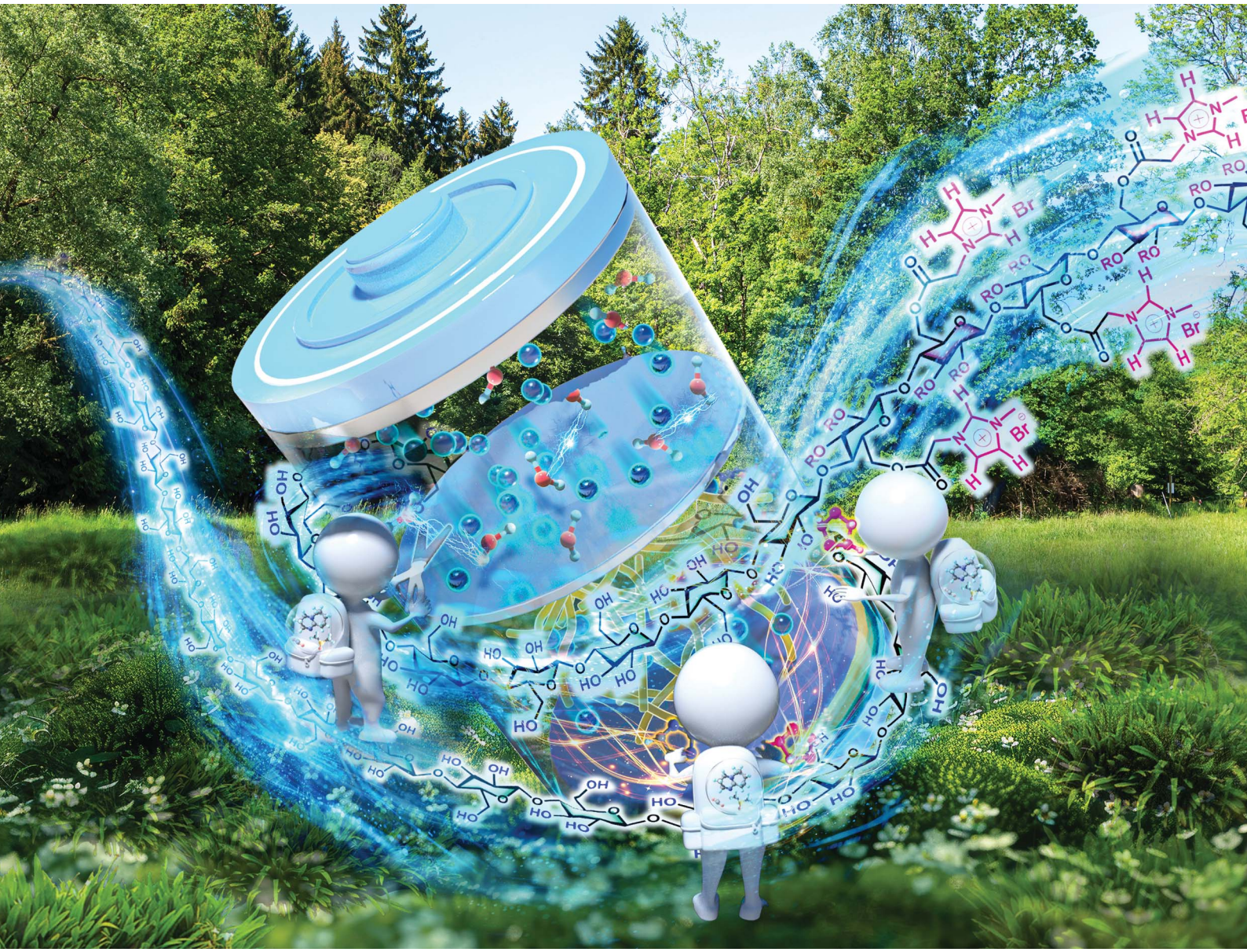

ISSN 2041-6539

ROYAL SOCIETY OF CHEMISTRY

EDGE ARTICLE

Haibo Xie *et al.*

Design of cellulosic poly(ionic liquid)s with a hydrogen bond/ion dual regulation mechanism for highly reversible Zn anodes

15 YEARS ANNIVERSARY

Chemical Science

ROYAL SOCIETY OF CHEMISTRY

EDGE ARTICLE

View Article Online
View Journal | View Issue

Cite this: *Chem. Sci.*, 2025, **16**, 8648

All publication charges for this article have been paid for by the Royal Society of Chemistry

Design of cellulosic poly(ionic liquid)s with a hydrogen bond/ion dual regulation mechanism for highly reversible Zn anodes†

Kui Chen,[ab] Yongzhen Xu,[ab] Hebang Li,[ab] Yue Li,[ab] Lihua Zhang,[ab] Yuanlong Guo,[ab] Qinqin Xu,[ab] Yunqi Li[ab] and Haibo Xie *[ab]

Received 26th February 2025
Accepted 9th April 2025

DOI: 10.1039/d5sc01555c

rsc.li/chemical-science

The unstable electrode/electrolyte interface with erratic zinc (Zn) deposition, severe dendritic growth and parasitic side reactions deteriorates the reversibility, tolerance and sustainability of aqueous Zn ion batteries (AZIBs). Herein, an imidazolium-based cellulosic poly(ionic liquid) ([CellMim]$^+$) additive with a hydrogen bond/ion dual regulation mechanism for aqueous electrolyte is designed and prepared *via* a transesterification reaction by considering particular solvent properties. The water-rich Zn anode interface is significantly optimized by hydrogen bond (HB) formation and preferential adsorption of [CellMim]$^+$. Additionally, the overfed Zn^{2+} ions are modulated by [CellMim]$^+$ cations though electrostatic repulsion, fostering uniform Zn deposition and a solid electrolyte interface (SEI). Notably, the Zn||Zn cells with [CellMim]$^+$ modified $Zn(OTf)_2$ electrolyte exhibit a long cycle life over 1800 h at 1 mA cm^{-2} and a high cumulative capacity of 3700 mA h cm^{-2} at 10 mA cm^{-2} with 56.9% Zn utilization rate (ZUR). Intriguingly, this electrolyte demonstrates a remarkable durability of 260 h at 8 mA cm^{-2} with 22.77% ZUR for a 9 cm^2 pouch cell. These results highlight the great potential of cellulosic derivatives in battery applications and offer valuable insights into the design of sustainable aqueous electrolyte additives for AZIBs.

Introduction

Rechargeable aqueous Zn ion batteries (AZIBs) are gaining considerable attention for applications ranging from electric vehicles to portable electronics due to their safety, cost-effectiveness, and environmental compatibility.[1–4] Unlike the flammable organic electrolytes used in lithium-ion batteries (LIBs), AZIBs employ aqueous electrolytes, significantly enhancing the safety while supporting fast charge and discharge rates.[5,6] Additionally, employing Zn metal as the anode provides benefits for sustainable development, given the natural abundance and compatibility of Zn with water.[7,8] However, AZIBs still face significant challenges regarding long-term stability and cycling reversibility due to water decomposition and irreversible Zn deposition.[9,10] Traditional electrolytes present shortcomings in that free water molecules within the electrolyte easily react with the Zn anode, resulting in undesirable side reactions (*e.g.*, Zn dendrite formation and the hydrogen evolution reaction (HER)).[11–13] These side effects not only reduce the battery lifespan but also pose safety risks, highlighting the need for advanced electrolyte strategies to improve the durability and reliability of AZIBs.

To tackle these challenges, ongoing studies are centered on functional electrolyte additives designed to regulate the hydrogen bond (HB), ion diffusion, electric field, electrical double layer and solid electrolyte interphase (SEI), ultimately achieving high reversibility of Zn anodes.[14–17] Among these additives, ionic liquids (ILs), eco-friendly solvents with distinctive anions and cations, have been effectively utilized in AZIBs to improve battery performance in the past few decades.[18] For example, Liao *et al.* used the 1-ethyl-3-methylimidazolium trifluoromethanesulfonate (EMImTfO) IL as three-dimensional inert-cation diversion dam to suppress Zn pulverization.[19] The EMIm$^+$ ions form a Galton-board-like cation-rich region on the Zn anode surface, serving as elastic sites to homogenize Zn^{2+} ion diffusion in an approximate Gaussian distribution, thereby greatly boosting the reversibility and stability. Similarly, Xu *et al.* introduced the 1-carboxymethyl-3-methylimidazolium chloride (CMIM) IL as a paradigm electrolyte additive to construct a stable *in situ* SEI by the synergistic effect of spontaneous electrostatic interactions and electrochemical decomposition.[20] The SEI with an organic-rich upper layer and an inorganic-rich inner layer enables uniform Zn^{2+} ion transport, high Zn utilization and record-breaking reversibility. Moreover,

[a]*Department of Polymeric Materials & Engineering, College of Materials & Metallurgy, Guizhou University, Huaxi District, Guiyang 550025, P. R. China. E-mail: hbxie@gzu.edu.cn*

[b]*Technology Innovation Center for High-Efficiency Utilization of Bamboo-Based Biomass in Guizhou Province, Guiyang 550025, China*

† Electronic supplementary information (ESI) available. See DOI: https://doi.org/10.1039/d5sc01555c

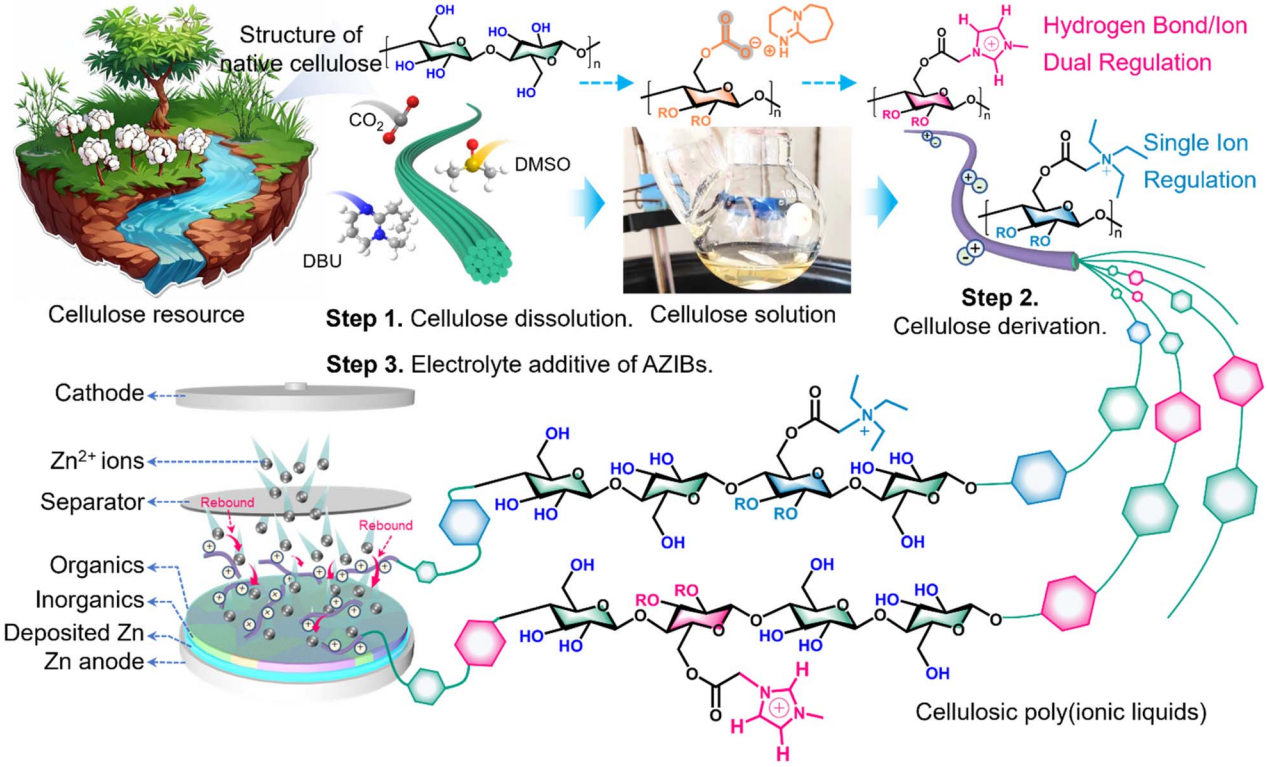

Fig. 1 Schematic diagram for the fabrication of the cellulosic PIL electrolyte additive. Step 1: dissolve cellulose in the DBU/CO_2/DMSO system. Step 2: *in situ* derivatization of cellulosic PILs. Step 3: coupling hydrogen bond/ion dual regulation mechanism for highly reversible Zn anodes.

Peng *et al.* introduced poly(diallyldimethylammonium chloride) (PDD) to regulate the electric fields of the Zn/electrolyte interface, enhancing Zn^{2+} ion migration and promoting preferential Zn (002) deposition.[21] Although these IL additive strategies have achieved significant progress, they have largely overlooked the role of the cation moiety in regulating HBs within the bulk electrolytes. In contrast, additives such as alcohols (*e.g.*, methanol,[22] triethylene glycol,[23] and xylitol[24]) and saccharides (*e.g.*, glucose[25] and trehalose[26]) excel in HB manipulation. Therefore, combining the ion-regulating properties of ILs with the HB-manipulating capabilities of hydroxyl-rich ligands is highly desirable yet very challenging.

Cellulose, a natural polymer rich in hydroxyl groups, offers a versatile platform for molecular design and synchronously provides an array of hydrogen-bonding sites.[27,28] Additionally, the imidazolium-based ILs, characterized by their imidazolium rings, engage in both nitrogen-mediated hydrogen bonding and proton-mediated hydrogen bonding, providing a more complex and effective HB interaction network.[29] Intrinsically, imidazolium-based ILs with a stable positive charge enhance the ionic conductivity and stability in aqueous environments, effectively mitigating Zn dendrite formation and suppressing the HER. Based on the above considerations, we propose using cellulose as a foundation and ILs as functional building blocks to design and synthesize a cellulosic poly(ionic liquid) (PIL) additive with a hydrogen bond/ion dual regulation mechanism, aiming to address the challenges faced by AZIBs more effectively.

Therefore, this article presents a molecular engineering strategy that transforms inert cellulose into an active host for high-performance electrolyte additives in AZIBs. Taking the particular solvent properties of the DBU/CO_2/DMSO solvent system, cellulose converts to a novel imidazolium-based cellulosic poly(ionic liquid) ($[CellMim]^+$) additive by a homogeneous transesterification reaction without adding any additional catalyst (Fig. 1). The $[CellMim]^+$ additive possesses superior ability for HB reconstruction, Zn^{2+} ion redistribution and driving SEI formation. As expected, Zn||Zn symmetric cells reveal a long life over 1800 h at 1 mA cm^{-2} and a high cumulative capacity of 3700 mA h cm^{-2} with a high ZUR of 56.9%. The resulting Zn||Zn pouch cell (9 cm^2) with $[CellMim]^+$ modified electrolyte runs stably for 260 h at 8 mA cm^{-2} with a ZUR of 22.77%. Moreover, the Zn||NVO batteries with this electrolyte maintain 83.6% capacity with a CE of >99.9% for 500 cycles at 1 A g^{-1}. This work provides insights for achieving high-performance AZIBs through a sustainable cellulosic PIL electrolyte additive triggered hydrogen bond/ion dual regulation mechanism.

Results and discussion

Design principle and structural characterization of cellulosic PILs

To validate the multiple hydrogen bonding capabilities of an imidazolium-based cellulosic poly(ionic liquid) ($[CellMim]^+$), a comparative counterpart of triethylamine-based cellulosic

poly(ionic liquid) ([CellEt$_3$N]$^+$) was designed and synthesized. Initially, two small-molecule ionic liquid (IL) precursors, a triethylamine-based IL and an imidazolium-based IL with distinct structural characteristics, were obtained from the alkylation reaction (Scheme 1, ESI†). Their structures were validated by ^{1}H and ^{13}C nuclear magnetic resonance (^{1}H- and ^{13}C-NMR) spectra (Fig. S1 and S2, ESI†). Subsequently, microcrystalline cellulose (MCC) was dissolved in the DBU/DMSO/CO_2 system, forming a transparent solution for efficient molecular-scale grafting (Scheme 2, ESI†). After esterification, [CellEt$_3$N]$^+$ and [CellMim]$^+$ were characterized by ^{1}H-NMR and ^{13}C-NMR. The ^{1}H-NMR spectra of [CellEt$_3$N]$^+$ and [CellMim]$^+$ show that chemical shifts between 2.8 and 5.5 ppm correspond to the protons of the cellulosic backbone,[30] resulting in degrees of substitution (DS) of 1.00 and 0.48, respectively (Fig. S3 and S4, ESI†). The ^{13}C-NMR spectra of [CellEt$_3$N]$^+$ and [CellMim]$^+$ also proved the identity of the obtained cellulosic PILs. Moreover, the Fourier transform infrared (FTIR) spectra of [CellEt$_3$N]$^+$ and [CellMim]$^+$ show an obvious new absorption peak located at 1756 cm^{-1}, which can be attributed to C=O stretching vibration of the newly formed ester group based on transesterification (Fig. S5, ESI†). Also, the absorption peaks of triethylamine and imidazolium salt appear in the corresponding spectra. Notably, the absorption peak between 3800 and 3000 cm^{-1} representing the hydrogen bond (HB) being widened and shifted to a high wavenumber, suggesting that the HBs among the cellulose chains in cellulosic PILs were weakened, which verified the HB reconstruction during the dissolution and derivatization process.[31] These results demonstrate the successful process of converting inert cellulose into cellulosic poly(ionic liquid)s.

Density functional theory (DFT) calculations were performed to generate electrostatic potential (ESP) maps, allowing visualization of the charge distribution around the H_2O molecule and cellulosic PILs (Fig. 2a). [CellMim]$^+$ shows strong polarity (4.93

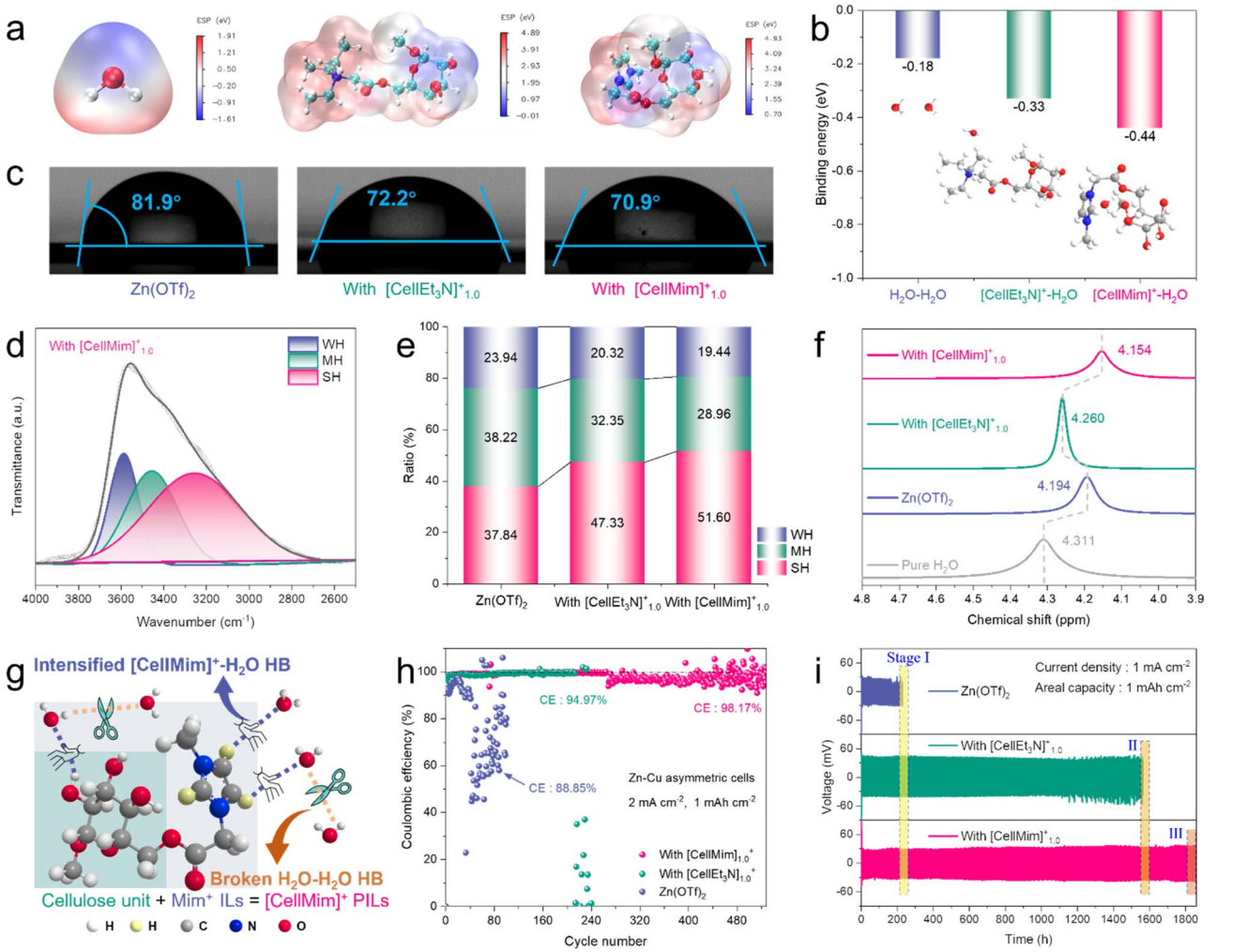

Fig. 2 (a) ESP maps of H_2O, [CellEt$_3$N]$^+$ and [CellMim]$^+$. (b) Binding energies of H_2O–H_2O, [CellEt$_3$N]$^+$–H_2O and [CellMim]$^+$–H_2O. (c) The contact angles of $Zn(OTf)_2$, $Zn(OTf)_2$ with [CellEt$_3$N]$_{1.0}^+$ and $Zn(OTf)_2$ with [CellMim]$_{1.0}^+$ electrolytes on Zn foil. (d) FTIR spectra of $Zn(OTf)_2$ with [CellMim]$_{1.0}^+$ electrolyte with typically fitted profiles. (e) Ratios of strong H-bond, medium H-bond, and weak H-bond in $Zn(OTf)_2$, $Zn(OTf)_2$ with [CellEt$_3$N]$_{1.0}^+$ and $Zn(OTf)_2$ with [CellMim]$_{1.0}^+$ electrolytes. (f) Comparison of chemical shifts of pure H_2O, $Zn(OTf)_2$, $Zn(OTf)_2$ with [CellEt$_3$N]$_{1.0}^+$ and $Zn(OTf)_2$ with [CellMim]$_{1.0}^+$ electrolytes. (g) Schematic of the effect of [CellMim]$^+$ on HBs in electrolytes. (h) The CEs of Zn||Cu cells using different electrolytes at 2 mA cm^{-2} and 1 mA h cm^{-2}. (i) Zn plating/stripping voltage profiles of Zn||Zn cells using different electrolytes at 1 mA cm^{-2} and 1 mA h cm^{-2}.

eV), which creates a higher driving force for the reconstruction of HBs than weak polar H_2O (1.91 eV) and medium polar $[CellEt_3N]^+$ (4.89 eV). This trend was further confirmed by calculating interaction energies of H_2O–H_2O and cellulosic PILs–H_2O pairs, where $[CellMim]^+$ shows the highest binding energy with H_2O, followed by $[CellEt_3N]^+$–H_2O and H_2O–H_2O in descending order (Fig. 2b). The contact angles of $Zn(OTf)_2$, $Zn(OTf)_2$ with $[CellEt_3N]_{1.0}^+$ and $Zn(OTf)_2$ with $[CellMim]_{1.0}^+$ electrolytes on Zn foil were 81.9°, 72.2° and 70.9°, respectively, demonstrating improved Zn affinity due to the polar groups of cellulosic PILs (Fig. 2c). Additionally, FTIR and ^{1}H-NMR analyses of $Zn(OTf)_2$, $Zn(OTf)_2$ with $[CellEt_3N]_{1.0}^+$ and $Zn(OTf)_2$ with [CellMim][Br] electrolytes were performed to reveal the manipulable HB interactions. The FTIR spectra of $Zn(OTf)_2$, $Zn(OTf)_2$ with $[CellEt_3N]_{1.0}^+$ and $Zn(OTf)_2$ with $[CellMim]_{1.0}^+$ electrolytes indicate an enhancement in H–O stretching vibration and a slight red shift in $CF_3SO_3^-$ (Fig. S6, ESI†). Specifically, the H–O stretching vibration of electrolytes can be deconvoluted into three distinctive peaks (Fig. 2d and S7, ESI†). The observed O–H stretching peaks at 3557.8 cm^{-1} (weak hydrogen bonds, WH), 3394.9 cm^{-1} (moderate hydrogen bonds, MH), and 3209.6 cm^{-1} (strong hydrogen bonds, SH) correlate with distinct hydrogen-bonding environments in the aqueous network. The increasing full width at half maximum (FWHM) from WH to SH reflects progressive vibrational coupling and dynamic disorder: (1) narrow WH peaks (*e.g.*, 3557.8 cm^{-1}) arise from loosely connected multimeric H_2O with minimal damping, resembling isolated oscillators; (2) intermediate MH peaks (*e.g.*, 3394.9 cm^{-1}) correspond to partially ordered hydration structures with moderate coupling; (3) broad SH peaks (*e.g.*, 3209.6 cm^{-1}) stem from tightly coordinated networks where strong H-bonding induces energy dissipation through collective vibrational modes and structural heterogeneity. This FWHM hierarchy aligns with established spectroscopic principles governing hydrogen-bond strength in aqueous systems.[20,32,33] The ratio of WH and MH decreased from 23.94% and 38.22% to 19.44% and 28.96%, respectively (Fig. 2e). Meanwhile, the SH ratio increased from 37.84% to 51.60% upon the addition of $[CellMim]_{1.0}^+$ to $Zn(OTf)_2$ electrolyte, further demonstrating that cellulosic PILs with SH reshape the HB network of H_2O. Moreover, a series of transparent and brown aqueous electrolytes with different concentrations of $[CellEt_3N]^+$ and $[CellMim]^+$ were fabricated (Fig. S8, ESI†). The ^{1}H-NMR signal shifts to higher magnetic fields after the addition of $[CellEt_3N]^+$ and $[CellMim]^+$, which suggests that the HBs among H_2O molecules are weakened (Fig. S9, ESI†).[34] The greater shift to a high magnetic field confirms that the HBs between $[CellMim]^+$ and H_2O (4.146 ppm) are stronger than those between $[CellEt_3N]^+$ and H_2O (4.252 ppm) (Fig. 2f). The difference is primarily attributed to the stronger hydrogen-bonding donor capability of the N-1 hydrogen atom in $[CellMim]^+$ compared to that in $[CellEt_3N]^+$. Therefore, the HBs between $[CellMim]^+$ and H_2O are strengthened, while the initial HBs among H_2O–H_2O are disrupted, as illustrated in Fig. 2g.

The ionic conductivity of these electrolytes was measured by assembling two pieces of Pt foil into an open half cell of a quartz cell (Fig. S10a, ESI†). The ionic conductivity slightly diminishes, with 49.80 mS cm^{-1} for pristine $Zn(OTf)_2$ electrolyte, 47.64 mS cm^{-1} for $Zn(OTf)_2$ with $[CellEt_3N]_{1.0}^+$ electrolyte and 49.01 mS cm^{-1} for $Zn(OTf)_2$ with $[CellMim]_{1.0}^+$ electrolyte, maintaining the merits of high ionic conductivity (Fig. S10b, ESI†). Encouragingly, $Zn(OTf)_2$ with $[CellEt_3N]_{1.0}^+$ and $Zn(OTf)_2$ with $[CellMim]_{1.0}^+$ electrolytes possess smaller corrosion current and more positive corrosion potential than pristine $Zn(OTf)_2$, which contribute to the protection of the Zn anode from active water intrusion in dilute electrolyte (Fig. S11, ESI†). Furthermore, the Zn||Cu asymmetrical cells and Zn||Zn symmetrical cells were used to evaluate reversibility of the Zn anode in these electrolytes. The $[CellMim]_{1.0}^+$ additive significantly boosts the coulombic efficiency (CE) of Zn plating/stripping, achieving an average CE of 98.17% and maintaining stable polarization voltage over 528 cycles in $Zn(OTf)_2$ with $[CellMim]_{1.0}^+$ electrolyte at 2 mA cm^{-2}/1 mA h cm^{-2} (Fig. 2h). The cell using pristine $Zn(OTf)_2$ electrolyte exhibits a rather low CE of 88.85% with a limited cycle life of only 32 cycles. However, a moderate CE of 94.97% was obtained in $Zn(OTf)_2$ with $[CellEt_3N]_{1.0}^+$ electrolyte, with the cycling life extended to 213 cycles. The same trend was tested at an increased current density of 5 mA cm^{-2} (Fig. S12, ESI†). The selected voltage profiles verify the enhanced reversibility of Zn stripping/plating, with no significant overpotential polarization observed throughout the entire 480 cycles in the $Zn(OTf)_2$ with $[CellMim]_{1.0}^+$ electrolyte. To further evaluate the reversibility, the Zn||Zn symmetric cells using $[CellEt_3N]_{1.0}^+$ and $[CellMim]_{1.0}^+$ modified electrolytes can sustain for 1560 h and 1860 h at 1 mA cm^{-2}, respectively (Fig. 2i and S13, ESI†). By comparison, the cell with pristine $Zn(OTf)_2$ electrolyte lasts for only 230 h before experiencing a battery short circuit. The improvement of excellent reversibility may be attributed to the strong Zn affinity, uniform electric field and Zn^{2+} flux imparted by cellulosic PIL additives ($[CellEt_3N]^+$ and $[CellMim]^+$), which will be further discussed later. Moreover, the above results confirmed that $[CellMim]^+$ modified electrolyte exhibited the best performance. Thus, $[CellMim]^+$ is considered as the optimal additive. The underlying reason is that $[CellMim]^+$ with three additional H protons on the imidazole ring can provide more HB sites than $[CellEt_3N]^+$, which helps reorganize the internal HB of the electrolyte, thereby suppressing side reactions.[35]

In addition, $[CellMim]^+$ additive concentration screening was still evaluated by Zn||Zn and Zn||Cu cells. Notably, the $Zn(OTf)_2$ with $[CellMim]_{1.0}^+$ electrolyte exhibits superior cycling over 760 cycles with the highest CE of 99.08% at 0.5 mA cm^{-2}, outperforming electrolytes with 0, 0.5 and 2.0 g L^{-1} additives (Fig. S14, ESI†). And the corresponding voltage capacity curves of the Zn||Cu cell employing $Zn(OTf)_2$ with $[CellMim]_{1.0}^+$ electrolyte almost completely overlap, symbolizing a high CE (Fig. S15, ESI†). Insufficient additives restrict the regulation of Zn^{2+}, while excessive additives increase the electrolyte's viscosity, leading to higher nucleation overpotentials (Fig. S16, ESI†). Consequently, the ideal concentration of $[CellMim]^+$ has been established as 1.0 g L^{-1}. Similar results were also observed in Zn||Zn symmetrical cells at 1 mA cm^{-2}, where the Zn||Zn cell using $Zn(OTf)_2$ with $[CellMim]_{1.0}^+$ electrolyte operates for over 1800 h, significantly outperforming cells employing the pristine $Zn(OTf)_2$ electrolyte and other concentrations of electrolytes (Fig. S17 and S18, ESI†).

Electrochemical performances of Zn electrodes

To clarify the Zn/electrolyte interface interaction, the interactions between the (002) crystal plane of Zn slab and $[CellMim]^+$ molecules were investigated by DFT calculations. As expected, the adsorption energy of $[CellMim]^+$ molecules on the Zn slab (002) crystal plane is as high as −3.53 eV, which is much larger than that of the H_2O molecule (−0.27 eV) (Fig. 3a and S19, ESI†).

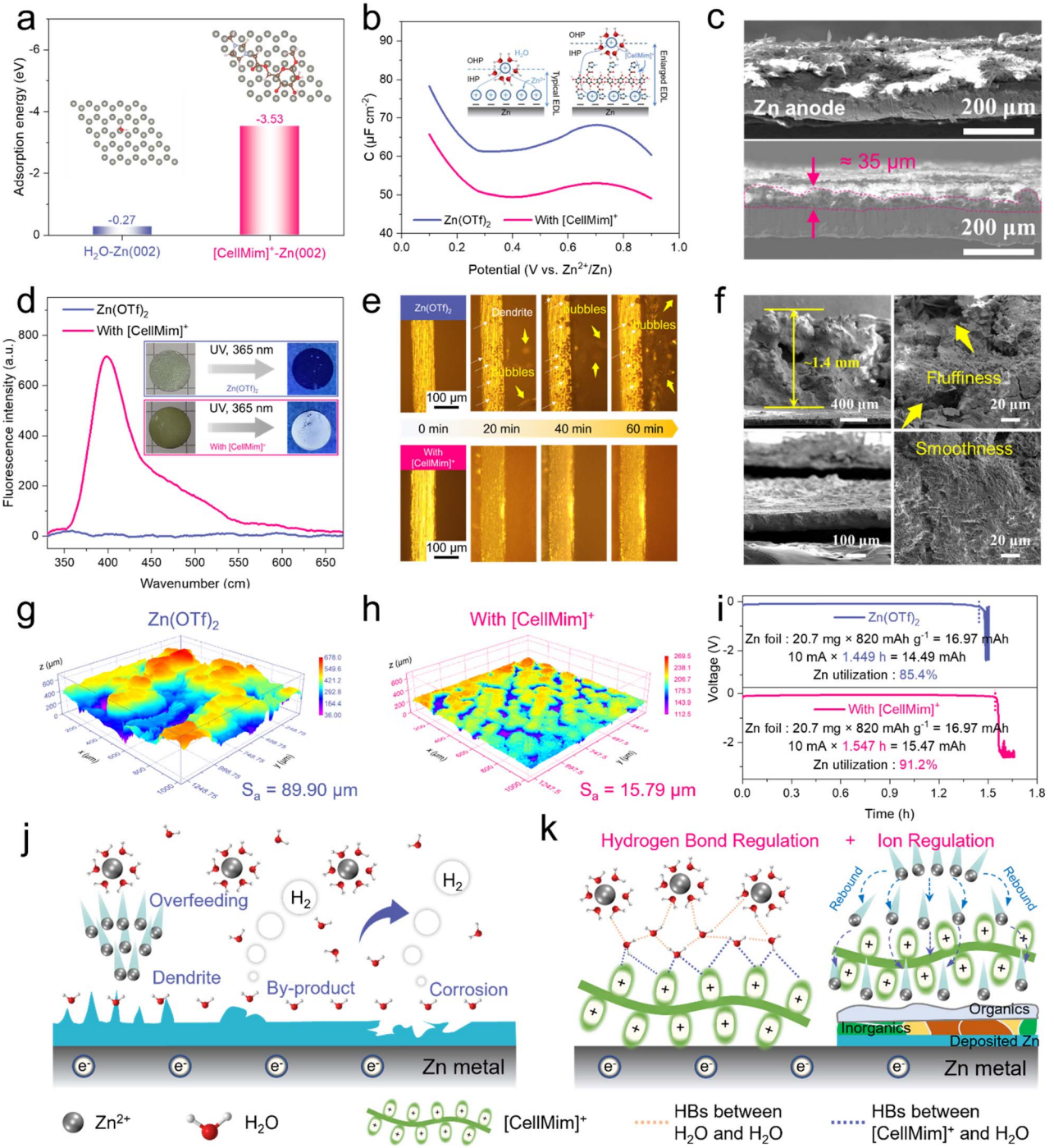

Fig. 3 (a) Adsorption energies of the Zn (002) plane with H_2O and $[CellMim]^+$. (b) Differential capacitance curves of Zn||Ti half cells using $Zn(OTf)_2$ and $Zn(OTf)_2$ with $[CellMim]^+$ electrolytes. (c) Cross-section SEM images of Zn foil after immersion in different electrolytes for 10 days. (d) Fluorescence spectra of $Zn(OTf)_2$ and $Zn(OTf)_2$ with $[CellMim]^+$ electrolytes under 353 nm excitation light. The illustrations are soaked pieces of Zn foil under 365 nm UV light irradiation. (e) *In situ* optical microscopy images of the Zn deposition process at 10 mA cm^{-2} in different electrolytes. (f) The cross-section and surface SEM images of the Zn anode after Zn deposition for 60 min. The 3D CLSM images after Zn deposition for 60 min at 10 mA cm^{-2} in (g) $Zn(OTf)_2$ and (h) $Zn(OTf)_2$ with $[CellMim]^+$ electrolytes. (i) Cumulative plating test for Zn||Zn symmetric cells using $Zn(OTf)_2$ and $Zn(OTf)_2$ with $[CellMim]^+$ electrolytes. (j and k) Schematic illustration of the evolution process during Zn deposition and SEI generation in these electrolytes.

This result indicates that $[CellMim]^+$ cations preferentially adsorb on the Zn anode, thereby preventing H_2O adsorption and inhibiting side reactions. The differential charge density distribution of the optimized adsorption configurations reveals that the electron cloud between Zn atoms and O/N atoms overlaps in Zn (002)-oriented $[CellMim]^+$ (Fig. S20, ESI†).[36] The strong adsorption of $[CellMim]^+$ cations is also assessed through phase selective alternating current voltammetry curves (Fig. 3b). With the introduction of $[CellMim]^+$, the capacitance at the interface decreases due to the preferential adsorption of large-sized cellulose units on the Zn anode surface, which broadens the EDL (illustration).[37] Also, the electric double layer capacitance (EDLC) can visually manifest the true surface area of the Zn anode, and if $[CellMim]^+$ cations repel water molecules to occupy the double layer, the value of EDLC will be changed.[38] According to the equation: $EDLC = (\varepsilon A)/d$, where ε is the dielectric constant of the electrolyte, A is the surface area of the Zn electrode, and d is the thickness of EDL, a larger d value will result in a smaller EDLC.[39] The EDLC value of the Zn electrode in pristine $Zn(OTf)_2$ electrolyte is 28.21 μF cm^{-2}, while a smaller EDLC value of 25.77 μF cm^{-2} is observed in $[CellMim]^+$ modified electrolyte, further confirming the preferential adsorption of $[CellMim]^+$ cations (Fig. S21, ESI†). The frontier orbital theory indicates that the narrow band gap between the lowest unoccupied molecular orbital (LUMO) and the highest occupied molecular orbital (HOMO) represents a favorable electron transfer tendency, which in turn facilitates the binding of molecules to the Zn slab.[40] $[CellMim]^+$ cations exhibit the smallest band gap of 7.98 eV, suggesting preferential adsorption of $[CellMim]^+$ cations on the Zn slab (Fig. S22, ESI†).

To further illustrate whether $[CellMim]^+$ cations are indeed preferentially absorbed on the Zn anode surface, the immersion experiment was performed. After soaking in pristine $Zn(OTf)_2$ electrolyte for 10 days, Zn foil exhibits a morphology characterized by massive flaky dendrites (Fig. 3c, top and Fig. S23a and b, ESI†), which can be indexed to inert $Zn_xOTf_y(OH)_{2x-y}\cdot nH_2O$ corrosion products (Fig. S24a, ESI†). Conversely, Zn foil in $[CellMim]^+$ modified electrolyte still presents a relatively smooth surface with fine and crystallized by-products owing to the redistribution of Zn^{2+} ion deposition with an electrostatic repulsion mechanism by $[CellMim]^+$ cations (Fig. 3c, bottom and Fig. S23c and d, ESI†). Additionally, the Zn foil immersed in $[CellMim]^+$ modified electrolyte exhibits fluorescent properties under 365 nm ultraviolet light irradiation, as illustrated in Fig. 3d. Further analysis of these electrolytes' fluorescence spectra reveals that $[CellMim]^+$ modified electrolyte displays strong fluorescence intensity under 353 nm excitation light, likely due to the cellulose skeleton (Fig. 3d).[41] These results further confirm that $[CellMim]^+$ cations are effectively adsorbed on the Zn foil. The $I_{(002)}/I_{(100)}$ and $I_{(002)}/I_{(101)}$ ratios of Zn foil after soaking in $[CellMim]^+$ modified electrolyte were enhanced to 1.89 and 0.45, respectively (Fig. S24b, ESI†). Meanwhile, the type and valence of elements on the Zn foil surface were analyzed by X-ray photoelectron spectroscopy (XPS). The high-resolution N 1s spectrum displays no detectable N on the Zn foil soaked in $Zn(OTf)_2$ electrolyte (Fig. S25c, ESI†). In contrast, a peak corresponding to N–C/–HN_2 appears on the Zn foil soaked in the $[CellMim]^+$ modified electrolyte, identifying physical adsorption of $[CellMim]^+$ on the Zn surface. The crystallization by-products of $Zn(OH)_2$ and ZnO were detected in the high-resolution spectrum of O 1s, aligning well with the SEM results (Fig. S25d, ESI†).

The monitoring of the Zn^{2+} ion deposition process is an important window to visualize the influence of $[CellMim]^+$ on dendrite inhibition, corrosion resistance and HER inhibition by self-assembly *in situ* optical microscopy (Fig. S26, ESI†). Numerous crystal nuclei appear on the Zn anode after only 20 min of plating at 10 mA cm^{-2} and H_2 bubbles simultaneously emerge at the interface within the $Zn(OTf)_2$ electrolyte (Fig. 3e, top). Regarding $[CellMim]^+$ modified electrolyte, homogeneous zinc deposits and no bubbles were observed during the entire plating process due to the strengthened HB, uniform electric field and concentration field regulated by $[CellMim]^+$. This significant inhibition of the HER is also proved by the linear sweep voltammetry (LSV) curves (Fig. S27a, ESI†). Additionally, the higher nucleation overpotential (NOP) indicates the fine Zn nucleation and the constrained 2D diffusion of Zn^{2+} ions. The ΔNOP between two electrolytes is 70.2 mV, indicating 3D diffusion of Zn^{2+} ions in modified electrolyte (Fig. S27b, ESI†). The morphology of the Zn anode after plating for 1 h was further characterized by SEM. The fluffy and pulverized deposit by-products with about 1.4 mm thickness were accumulated on the Zn anode (Fig. 3f, top and Fig. S28a–c, ESI†). In contrast, the Zn anode maintains a dense and smooth surface after plating in $[CellMim]^+$ modified electrolyte and most of the flake dendrites are embedded in the polymer matrix, avoiding the risk of piercing the separator (Fig. 3f, bottom and Fig. S28d–f, ESI†). The 2D and 3D confocal laser scanning microscopy (CLSM) analyses were performed to further investigate the differences in Zn deposition. The Zn anode in $[CellMim]^+$ modified electrolyte exhibits a significantly lower surface roughness (S_a) of 15.79 μm, compared to 89.90 μm in $Zn(OTf)_2$ electrolyte (Fig. 3g and h). Additionally, the Zn anode in $Zn(OTf)_2$ electrolyte exhibits much higher line roughness (R_a) of 42.71 μm compared to 19.72 μm in $[CellMim]^+$ modified electrolyte (Fig. S29, ESI†). The corresponding roughness profiles were recorded, further highlighting the superior Zn deposition behavior facilitated by $[CellMim]^+$.

Furthermore, the cumulative plating measurement was used to accurately evaluate the inhibition effect on dendrite growth, the HER and corrosion by $[CellMim]^+$. Specifically, Zn||Zn cells with 30 μm Zn foil were subjected to a unilateral electroplating until the cells failed at a current of 10 mA (Fig. 3i). The Zn utilization is as high as 91.2% in $[CellMim]^+$ modified electrolyte, while only 85.4% Zn utilization is observed in $Zn(OTf)_2$ electrolyte. After the cumulative plating test, one side of the Zn electrode was completely dissolved (Fig. S30, ESI†). To visually observe the impact of $[CellMim]^+$ on inhibiting dendrites, a quartz cell with a transparent window was engaged to explore the Zn deposition behavior. After one plating and stripping at 10 mA cm^{-2} and 15 mA h cm^{-2}, the Zn deposit of electrode A (stripping first, then plating) in $[CellMim]^+$ modified electrolyte exhibits a flat crystal surface morphology (Fig. S31, ESI†). However, lamellar dendrites form in $Zn(OTf)_2$ electrolyte, which

are prone to detaching and result in poor reversibility (Fig. S32, ESI†). In electrode B (plating first, then stripping), severe dissolution of the Zn anode was noticed in the $Zn(OTf)_2$ electrolyte, suggesting an overfed Zn^{2+} ion flux during this charge–discharge cycle. This phenomenon strongly demonstrates that $[CellMim]^+$ can also regulate the Zn^{2+} ion deposition process through electrostatic repulsion interactions. The current intensity continued to increase throughout the process in the $Zn(OTf)_2$ electrolyte, indicating a prolonged duration of the 2D diffusion process (Fig. S33, ESI†). During 2D diffusion, Zn^{2+} ions migrate to the Zn anode surface, aggregating at high surface energy sites and growing into dendrites.[42] In contrast, the Zn^{2+} ion diffusion shows 3D diffusion dominance in the $[CellMim]^+$ modified electrolyte due to the constrained direct deposition by electrostatic repulsion interactions between Zn^{2+} ions and $[CellMim]^+$ cations.

In general, the formation of dendrites includes successive processes: Zn^{2+} diffusion, Zn^{2+} reduction, Zn nucleation and Zn crystal growth.[19,43] Consequently, Zn^{2+} ions are often overfed during battery operation under an applied electric field, leading to Zn atom accumulation that readily surpasses a critical threshold. In this scenario, the irreversible deposition of overfed Zn^{2+} ion flux and the continuous accumulation of Zn atoms at a high potential of the Zn anode further led to the formation of Zn dendrites (Fig. 3j). Moreover, the HER, corrosion and irreversible by-products will successively appear on the H_2O-rich electrode–electrolyte interface, which will further deteriorate the overall battery performance. To avoid the above dilemma, $[CellMim]^+$ acts as a regulator for Zn^{2+} ion migration, where the overfed Zn^{2+} ions are rebound in the bulk electrolyte through electrostatic repulsion interactions, ultimately achieving 3D diffusion of Zn^{2+} ions to the electrode surface (Fig. 3k). Besides, $[CellMim]^+$ cations tightly adsorbed on the Zn anode, crowding out active H_2O to form a H_2O-poor electrode–electrolyte interface. Also, $[CellMim]^+$-mediated hydrogen bonding inhibits side reactions induced by parasitic H_2O, further improving reversibility of the Zn anode.

To explore the positive function of the $[CellMim]^+$ additive, the Zn plating/stripping reversibility in $Zn(OTf)_2$ with and without $[CellMim]^+$ was systematically studied. The CE of the Zn‖Cu half cell was quantified to scrutinize the reversibility of the electrode in rechargeable batteries.[44] The Zn‖Cu cell using $[CellMim]^+$ modified electrolyte delivers an average CE of 98.31%, outperforming that of the Zn‖Cu cell using the $Zn(OTf)_2$ electrolyte (96.04%) (Fig. S34, ESI†). Furthermore, the XRD patterns of the Cu electrode vividly reveal the pronounced inhibition of Zn dendrite formation by $[CellMim]^+$ after 100 cycles in Zn‖Cu cells (Fig. S35, ESI†). The SEM image of the cycled Cu electrode in $Zn(OTf)_2$ electrolyte exhibits massive by-products and large flaky dendrites interwoven with glass fiber separators (Fig. S36a and b, ESI†). In contrast, the flat and clean Cu electrode surface reveals the improved reversibility by $[CellMim]^+$ (Fig. S36c and d, ESI†). Furthermore, the long-term cycling reversibility of Zn electrodes in these electrolytes was evaluated under various current densities and areal capacities of Zn‖Zn symmetric cells. The long-term cycle rate performance based on $[CellMim]^+$ modified electrolyte delivers a stable hysteresis voltage from 1 to 20 mA cm^{-2}, with a total cycling life of 876 h over 12 loops (Fig. 4a). Additionally, the exchange current, derived from rate measurements, was fitted and calculated (Fig. S37, ESI†). The exchange current density of the Zn‖Zn cell using $[CellMim]^+$ modified electrolyte (19.763 mA cm^{-2}) is higher than that of pristine $Zn(OTf)_2$ electrolyte (17.719 mA cm^{-2}), suggesting that $[CellMim]^+$ significantly improves reversibility (Fig. 4b). The improved electrochemical reversibility enables the Zn‖Zn symmetric cell with $[CellMim]^+$ modified electrolyte to operate for over 940 h at 3 mA cm^{-2}, in contrast to only 27 h in $Zn(OTf)_2$ electrolyte (Fig. S38, ESI†). Additionally, as the current density increases to 5 mA cm^{-2}, the Zn‖Zn cell survives for 2500 cycles with a cumulative capacity of 5000 mA h cm^{-2} in $[CellMim]^+$ modified electrolyte (Fig. S39, ESI†). In contrast, unstable hysteresis voltage lasts for the entire cycle period in $Zn(OTf)_2$ electrolyte, implying the continuous corrosion and dendrite growth. Under this condition, Zn anodes of different cycle stages were collected to systematically analyze the phase composition by XRD (Fig. S40, ESI†). The relative texture coefficients (RTCs) of (002), (100) and (101) crystal planes were calculated from the corresponding intensity values in Table S1.† The RTCs of both (002) and (101) crystal planes slightly decrease, while the RTC of the (100) crystal plane gradually intensifies, demonstrating the predominance of the unfavoured (100) crystal plane texture in the $Zn(OTf)_2$ electrolyte (Fig. 4c). By contrast, the RTCs of the Zn electrode in $[CellMim]^+$ modified electrolyte exhibit a significant increase of (002) crystal planes and a decrease of (100) and (101) crystal planes, consistent with SEM results (Fig. 4d and S41, ESI†). Further increasing the current density to 10 mA cm^{-2}, the symmetric cell using $[CellMim]^+$ modified electrolyte demonstrates a durable cycle life of 3350 cycles with a cumulative capacity of 6700 mA h cm^{-2}, more than 17 times higher than that of $Zn(OTf)_2$ electrolyte (Fig. S42, ESI†).

To study the endurance of AZIBs under extreme conditions, the long cycle performance of symmetric cells was also characterized at a high Zn utilization rate (ZUR).[45] After introducing the $[CellMim]^+$ additive, the Zn‖Zn symmetric cell can manifest much longer cycle lifespan of 300 h than an ordinary electrolyte with only 45 h at 5 mA cm^{-2} with a ZUR of 28.47% (Fig. S43, ESI†). On further increasing the current density, the Zn‖Zn cell using $[CellMim]^+$ modified electrolyte delivers an extended lifespan of over 420 h with a ZUR of 28.47% at 10 mA cm^{-2}, over 9-fold improvement of $Zn(OTf)_2$ electrolyte (45 h) (Fig. S44, ESI†). Besides, the cell achieves excellent cycling performance over 370 h even with a high ZUR of 56.93% at 10 mA cm^{-2}, which may be related to the robust solid electrolyte interphase (SEI) derived by $[CellMim]^+$ additives (Fig. 4e) (discussed later). For more comprehensive and reasonable evaluation of the symmetric cell performance, the life factors of the advanced literature are summarized in Fig. 4f and Table S2.† Impressively, our life factor exceeds 210, which is significantly superior to most state-of-the-art counterparts under harsh conditions. In order to be closer to the actual scenario of battery applications, the calendar aging test was carried out to measure the battery performance with the intermittent rest of 20 h (Fig. 4g). The Zn‖Zn cell with $[CellMim]^+$ modified electrolyte can operate

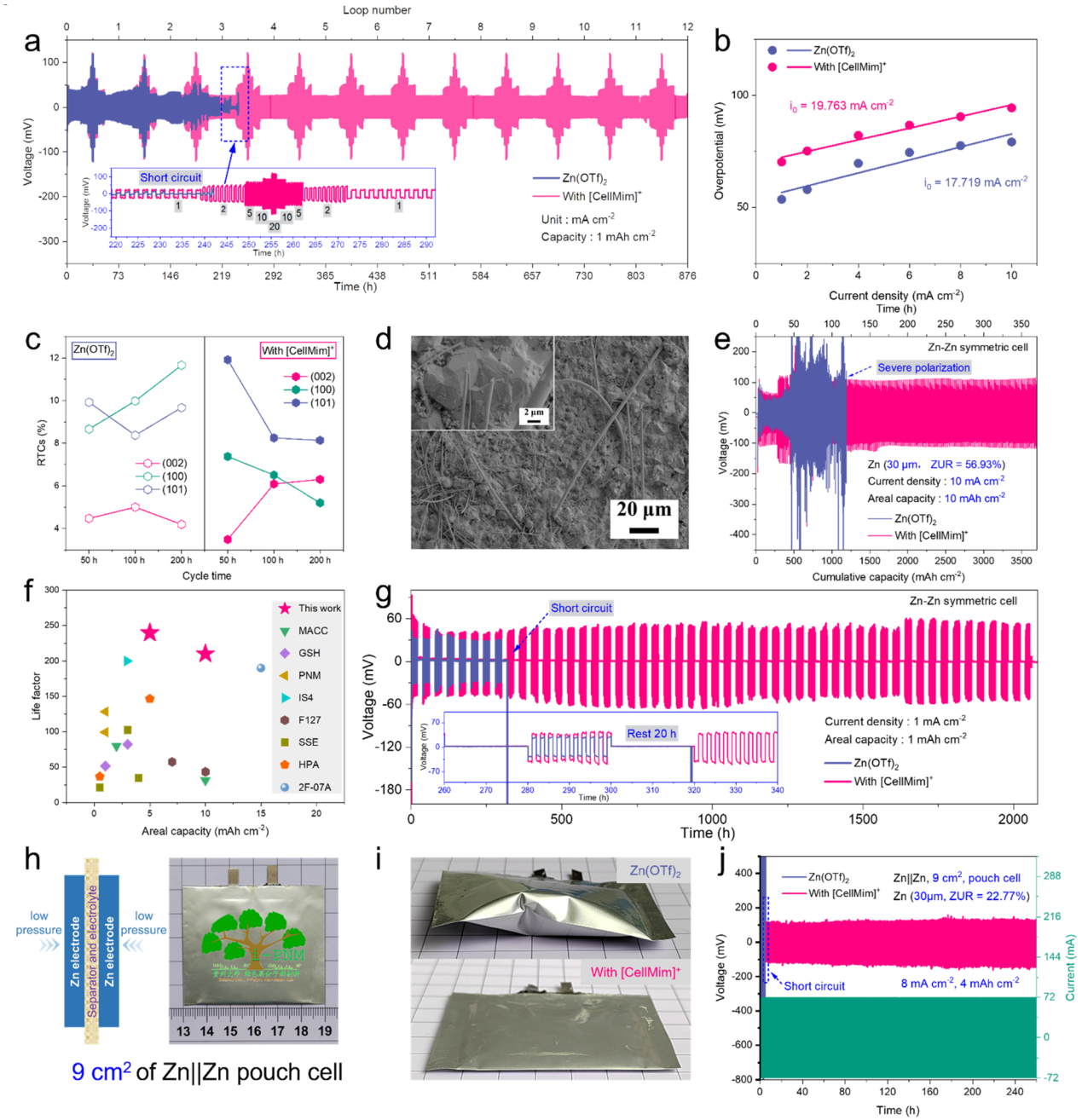

Fig. 4 (a) Rate performance and (b) calculated exchange current densities of Zn||Zn symmetric cells using different electrolytes. (c) RTCs of the Zn anode in Zn||Zn symmetric cells using different electrolytes as a function of cycle time at 5 mA cm^{-2} and 1 mA h cm^{-2}. (d) SEM image of the Zn anode in Zn||Zn symmetric cells using $Zn(OTf)_2$ with $[CellMim]^+$ electrolyte after 200 h of cycling at 5 mA cm^{-2} and 1 mA h cm^{-2}. (e) Cycling performance of Zn||Zn symmetric cells at 10 mA cm^{-2} and 10 mA h cm^{-2}. (f) The comparison of "life factors" between this work and previous reported studies. (g) Calendar life of Zn||Zn symmetric cells under 1 mA cm^{-2} and 1 mA h cm^{-2}. (h) Schematic and photograph of a Zn||Zn symmetric pouch cell. (i) The corresponding photos of Zn||Zn pouch cells after cycling at 5 mA cm^{-2} and 1 mA h cm^{-2}. (j) Long cycling performance of Zn||Zn pouch cells at 8 mA cm^{-2} and 4 mA h cm^{-2} with a ZUR of 22.77%.

with excellent long-term stability over 2000 h during the intermittent charge/discharge process. However, the cell can only operate for less than 320 h in $Zn(OTf)_2$ electrolyte, demonstrating enhanced reversibility and durability by $[CellMim]^+$. Similarly, the symmetrical cell achieved significant improvement at 3 mA cm^{-2} (Fig. S45, ESI†).

Given that there is an obvious difference between the coin cells and the pouch cells, the pouch cell with a thin Zn electrode, a high ZUR, low external force and small amount of electrolyte is a way to improve the practical high-performance of AZIBs.[46] We simply assembled a single-layer Zn||Zn symmetrical pouch cell with 30 μm-thick Zn foil (3 cm × 3 cm), 290 μm-thick glass fiber separator (4 cm × 4 cm) and 1.8 mL electrolyte in air.

The corresponding schematic diagram and photograph of a pouch cell are given in Fig. 4h. The pouch cell using [CellMim]$^+$ modified electrolyte can operate stably for 320 h at 1 mA cm^{-2} (Fig. S46, ESI†). In contrast, severe polarization occurs only after 64 h, attributed to the unstable electrode–electrolyte interface and severe HER. Additionally, the symmetrical pouch cell achieves a cumulative capacity of 1650 mA h cm^{-2} at 5 mA cm^{-2} with a ZUR of 5.68%, significantly outperforming the pristine $Zn(OTf)_2$ electrolyte, which experiences a soft short circuit at just 287 mA h cm^{-2} (Fig. S47, ESI†). The serious bulge of the pouch cell after cycling in the $Zn(OTf)_2$ electrolyte suggests that the inevitable HER severely consumes the electrolyte (Fig. 4i). When a current of 72 mA and ZUR of 22.77% are applied to the symmetric pouch cell, it was barely operational in the $Zn(OTf)_2$ electrolyte (Fig. 4j and S48, ESI†). However, it operated remarkably for 260 h in [CellMim]$^+$ modified electrolyte. Such excellent tolerance and reversibility can be ascribed to strengthened HB, enhanced self-adsorption, redistributed Zn^{2+} diffusion, and stable SEI formation. The preferential self-adsorption of [CellMim]$^+$ cations and sluggish diffusion of Zn^{2+} ions can be determined from the activation energy (E_a). The calculated E_a value in the Zn||Zn cell with [CellMim]$^+$ modified electrolyte is 45.30 kJ mol^{-1}, which is larger than 33.42 kJ mol^{-1} in the Zn||Zn cell with $Zn(OTf)_2$ electrolyte (Fig. S49, ESI†). This result indicates that [CellMim]$^+$ adsorbed at the interface leads to a higher energy barrier in Zn plating/stripping. Additionally, the electrostatic repulsion between Zn^{2+} cations and [CellMim]$^+$ cations also significantly alleviates the overfed Zn^{2+} ion flux and delays Zn^{2+} ion deposition kinetics.

To further understand the mechanism of concentration and electric field regulating Zn dendrite formation during Zn deposition, a phase field model of the electrochemical reaction was developed (Table S3, ESI†).[47] First, a small bump was introduced on the Zn metal surface to simulate the Zn crystal nucleus. As the Zn electrodeposition proceeded, the Zn protrusion grew along the vertical electrode surface (Fig. 5a). Subsequently, it rapidly evolved into a sharp Zn dendrite, which can be assigned to the "tip effect" exacerbated by the inhomogeneous electric field and Zn^{2+} ion concentration field in the $Zn(OTf)_2$ electrolyte system. In contrast, the initial Zn nuclei gradually formed a dome-like morphology with a smooth electrode electrolyte interface by regulation of the concentration field and electric field in the [CellMim]$^+$ modified electrolyte system (Fig. 5d). Moreover, the Zn^{2+} ion concentration–distance (along dendrite growth direction) and electric field–distance curves were further used to quantitatively analyze the growth process. In both systems, along the dendrite growth direction (illustration), the Zn^{2+} ion concentration and electric field intensity increased sharply and reached the maximum at the tip of the dendrite. Obviously, the Zn^{2+} ion concentration–distance curves and electric field–distance curves greatly shift to the right in the $Zn(OTf)_2$ system as the function of time (Fig. 5b, c and S50, ESI†), while the curves slightly shift in the [CellMim]$^+$ modified electrolyte system (Fig. 5e, f and S51, ESI†), suggesting a significantly inhibited dendrite growth. Importantly, the Zn dendrite growth rate (v) in the $Zn(OTf)_2$ system (0.009 μm s^{-1}) is much larger than that in the [CellMim]$^+$ modified electrolyte system (0.002 μm s^{-1}), which is an intuitive and significant result (Fig. S52, ESI†).

The robust SEI was first revealed by *in situ* electrochemical impedance spectroscopy (EIS). The symmetrical cells undergo a test procedure involving 3 minutes of discharging followed by 3 minutes of standing, with EIS data collected after each cycle (Fig. S53a, ESI†). The EIS spectrum shows a gradually decreasing interfacial transfer resistance (R_{ct}) in $Zn(OTf)_2$ electrolyte, suggesting the absence of SEI (Fig. S53b, ESI†). In contrast, R_{ct} increased slightly in the first 10 cycles, likely due to the adsorption of [CellMim]$^+$ cations, which increased the energy barrier of Zn^{2+} ion transport. In the following 10 cycles, R_{ct} decreased slightly, suggesting that the ionic-conductive inorganic SEI began to form (Fig. S53c, ESI†). On the other hand, high-resolution transmission electron microscopy (HRTEM) was employed to analyze the structure of the SEI. The high-angle annular dark-field image, along with the corresponding energy dispersive spectroscopy (EDS) mapping, reveals a uniform distribution of C, N, O, F, S and Zn elements throughout the SEI layer (Fig. 5g). Subsequently, the lattice fringes of SEI were analyzed by fast Fourier transform (FFT), and results show that three typical inorganic compounds of ZnF_2 (101), ZnF_2 (110) and $ZnCO_3$ (104) were accurately matching (Fig. 5h). This result confirms that a well-crystallized inorganic grain exists in the SEI, which is verified by the polycrystalline diffraction ring (illustration).

XPS depth analysis combined with Ar^+ sputtering was carried out to further identify the SEI composition (Fig. S54, ESI†). The C 1s signal on the surface of SEI can be decomposed into four species. The peaks at 292.9, 288.2, 286.4 and 284.8 eV were attributed to C–F, C–O═C, C–O/C–N and C–C/C–H bonds, respectively.[48] With Ar^+ sputtering, the signals of all species decrease sharply in C 1s, likely attributed to the surface adsorption of [CellMim]$^+$ cations and $CF_3SO_3^-$ anions (Fig. 5i). Moreover, the N 1s signal exists in the form of C–N/–NH_2^+ at 400.2 eV, which is attributed to the surface adsorption of [CellMim]$^+$ cations (Fig. 5j). Additionally, the O 1s fine spectrum proved that $ZnCO_3$ and $ZnSO_3$ existed in the entire SEI volume, and some dead Zn of ZnO and alkaline by-product of $Zn(OH)_2$ were also inevitably generated (Fig. S55a, ESI†). In F 1s and S 2p spectra, –CF_3 and SO_3^{2-} species gradually decreased and even disappeared, while the signals of ZnF_2 and ZnS species became stronger, suggesting that the inner layer of SEI is composed of inorganic components and the outer layer of SEI is dominated by organic components (Fig. 5k and S55b, ESI†). Therefore, a stable and robust hybrid SEI was constructed, which constitutes a well-crystallized inorganic-rich inner layer and surface adsorption of the [CellMim]$^+$-rich outer layer.

Electrochemical performances of Zn||$NH_4V_4O_{10}$ full batteries

To verify the feasibility of [CellMim]$^+$ in practical AZIBs, a Zn||$NH_4V_4O_{10}$ (NVO) full battery was assembled. The microstructure of NVO presents a banded cluster, and the EDS mapping confirmed an even distribution of N, O, and V throughout the cathode material (Fig. S56, ESI†). The XRD pattern of NVO power is well indexed to the ammonium

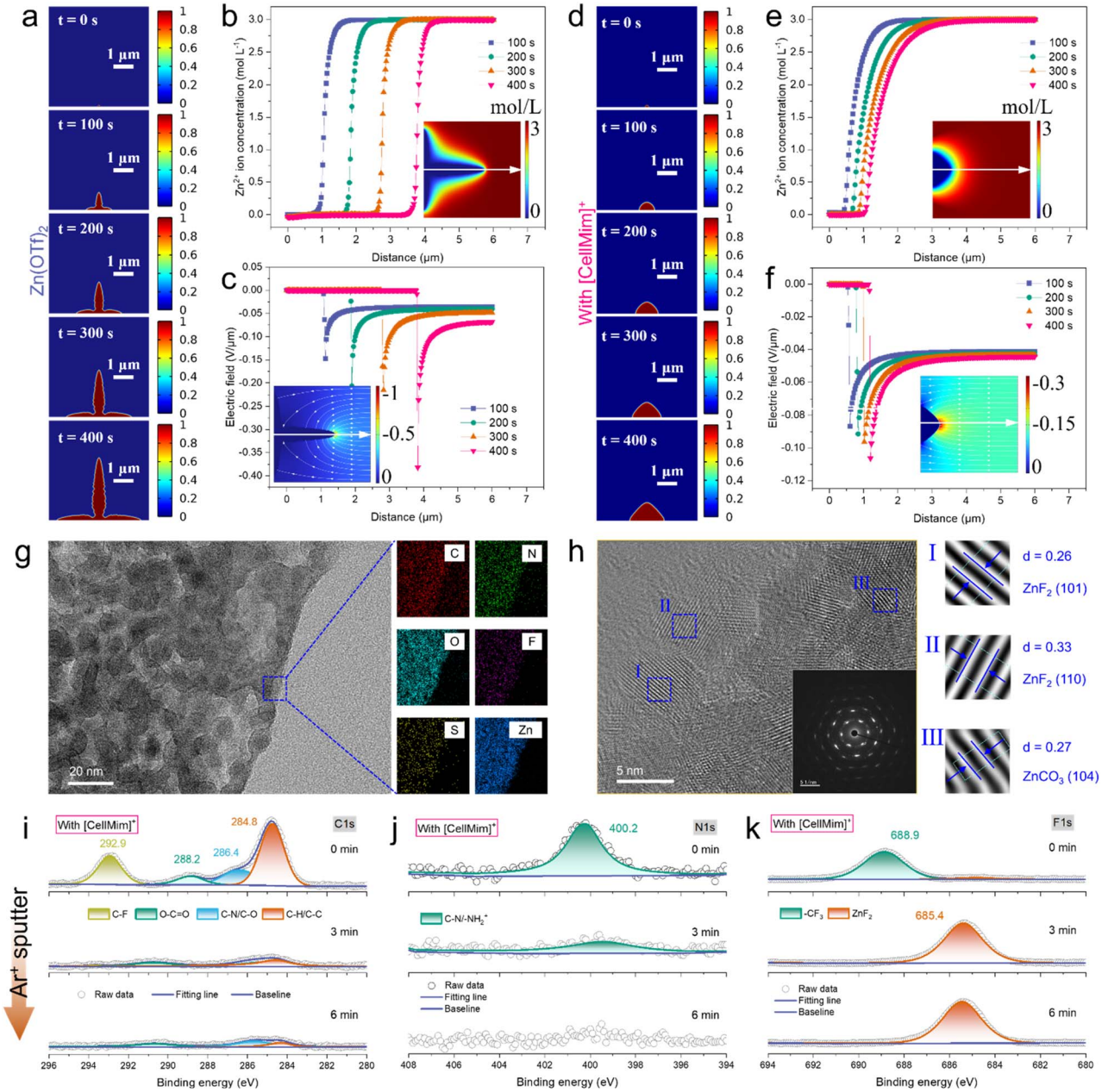

Fig. 5 Dendrite morphology growth as a function of time based on (a) $Zn(OTf)_2$ and (d) $Zn(OTf)_2$ with $[CellMim]^+$ electrolyte. 1D evolution of Zn^{2+} ion concentration profiles along the x-axis across the tip of the dendrite based on (b) $Zn(OTf)_2$ and (e) $Zn(OTf)_2$ with $[CellMim]^+$ electrolytes. The images in the inset show the 2D map of the Zn^{2+} ion concentration at $t = 400$ s. 1D evolution of electric field profiles along the x-axis across the tip of the dendrite based on (c) $Zn(OTf)_2$ and (f) $Zn(OTf)_2$ with $[CellMim]^+$ electrolytes. The images in the inset show the 2D distribution of the local electric field at $t = 400$ s. (g) TEM image and element mapping of the SEI formed in $Zn(OTf)_2$ with $[CellMim]^+$ electrolyte. (h) HRTEM image and diffraction rings of ZnF_2 (101), ZnF_2 (110) and $ZnCO_3$ within the SEI formed in $Zn(OTf)_2$ with $[CellMim]^+$ electrolyte. The XPS depth spectra of (i) C 1s, (j) N 1s and (k) F 1s of the Zn anode tested in a symmetric cell based on $Zn(OTf)_2$ with $[CellMim]^+$ electrolyte for 30 cycles at 5 mA cm^{-2} and 2 mA h cm^{-2}.

vanadate phase (PDF#18-0136) (Fig. S57, ESI†). The CV curves of the initial 5 cycles in Zn||NVO batteries show a gradually expanding area, representing an activation process of NVO (Fig. S58, ESI†). Additionally, the polarization at a high potential (1.6 V) gradually disappears. The CV curves at a scan rate of 0.2 mV s^{-1} in the voltage range of 0.3–1.6 V indicated that the $[CellMim]^+$ additive did not affect the energy storage mechanism (Fig. 6a). In particular, two pairs of obvious redox peaks were observed at 0.54/0.60 and 1.00/0.98 V, which were related to the redox reactions of V^{3+}/V^{4+} and V^{4+}/V^{5+}, respectively. The relatively weak peak pair at 1.43/1.33 V may be assigned to the multi-step deintercalation/intercalation process of Zn^{2+} ions in the V–O interlayer.[49] The CV curves of Zn||NVO batteries with those electrolytes at various scan rates from 0.2 to

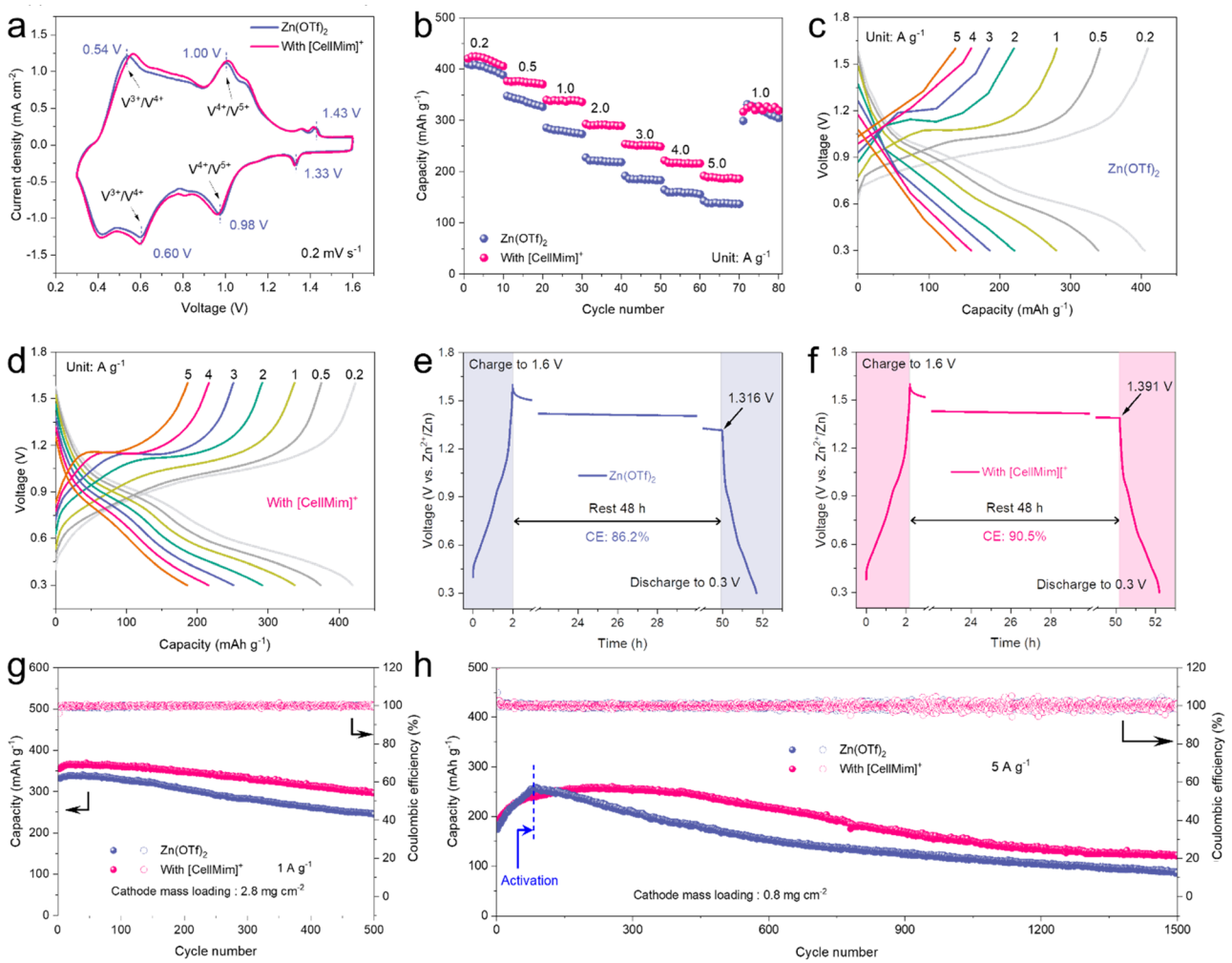

Fig. 6 Electrochemical performance of Zn||NVO full batteries. (a) The CV curves at 0.2 mV s^{-1}. (b) Rate performance of Zn||NVO batteries in $Zn(OTf)_2$ and $Zn(OTf)_2$ with $[CellMim]^+$ electrolytes. GCD profiles of Zn||NVO batteries using (c) $Zn(OTf)_2$ and (d) $Zn(OTf)_2$ with $[CellMim]^+$ electrolytes at various current densities from 0.2 to 5 A g^{-1}. Self-discharge curves of Zn||NVO batteries using (e) $Zn(OTf)_2$ and (f) $Zn(OTf)_2$ with $[CellMim]^+$ electrolytes at 0.2 A g^{-1}. Galvanostatic discharge/charge curves of Zn||NVO batteries using different electrolytes at (g) 1 A g^{-1} and (h) 5 A g^{-1}.

1.0 mV s^{-1} present a linear change, suggesting a non-destructive reversibility of the NVO cathode material by adding $[CellMim]^+$ (Fig. S59, ESI†).

The rate performance of the Zn||NVO full battery with $[CellMim]^+$ modified electrolyte delivers high specific capacities of 419.1, 373.9, 337.2, 291.7, 251.0, 215.7 and 186.0 mA h g^{-1} at 0.2, 0.5, 1, 2, 3, 4 and 5 A g^{-1}, respectively, which is better than $Zn(OTf)_2$ electrolyte (Fig. 6b–d and S60, ESI†). The self-discharge behavior was investigated by resting a fully charged battery for 48 h at 0.2 A g^{-1}, with the resulting CE serving as an indicator of the battery's interface stability. Encouragingly, $[CellMim]^+$ endow the Zn||NVO full batteries with a high CE of 90.5%, which exceeds that of the $Zn(OTf)_2$ electrolyte (86.2%) (Fig. 6e and f). After 48 h of resting, the voltage of the Zn||NVO battery with $Zn(OTf)_2$ electrolyte was reduced to 1.316 V, while that with $[CellMim]^+$ modified electrolyte had a higher voltage of 1.391 V. To align with typical practical application scenarios, the cycle life of Zn||NVO batteries was evaluated under low current densities.[50] The Zn||NVO battery employing $Zn(OTf)_2$ electrolyte exhibited rapid capacity decay at 0.2 A g^{-1}, ultimately undergoing short-circuit after 100 cycles (Fig. S61a, ESI†). In contrast, the counterpart utilizing $[CellMim]^+$ modified electrolyte demonstrated significantly enhanced cycling stability, retaining 67.4% of its initial capacity over 200 cycles. Also, the $[CellMim]^+$ modified system maintained 62.9% capacity retention after 300 cycles at 0.5 A g^{-1}, highlighting its superior electrochemical durability (Fig. S61b, ESI†). Benefiting from $[CellMim]^+$, the Zn||NVO battery has a stable capacity of 296.9 mA h g^{-1} after 500 cycles at 1 A g^{-1} (Fig. 6g), outperforming the battery without $[CellMim]^+$ (245.4 mA h g^{-1}). The corresponding galvanostatic charge/discharge (GCD) profiles were recorded (Fig. S62, ESI†). Additionally, the Zn||NVO battery with $[CellMim]^+$ modified electrolyte achieves a capacity retention of 68.7% after 1000 cycles at 3 A g^{-1} (Fig. S63, ESI†). Moreover, the Zn||NVO battery with $[CellMim]^+$ modified electrolyte delivers a maximum capacity of 255.7 mA h g^{-1} after 200 cycles of full

activation at 5 A g^{-1} and finally obtains a high capacity of 122.3 mA h g^{-1} (Fig. 6h and S64, ESI†). This designable cellulosic PIL additive exhibits huge potential for practical application in the AZIB domain and beyond.

Conclusions

In summary, our results highlight the potential of designable cellulosic PILs in the AZIB domain. Using the particular solvent properties of the DBU/CO_2/DMSO solvent system, inert cellulose was converted into high value-added $[CellMim]^+$ for aqueous electrolyte additives. The $[CellMim]^+$ developed here exhibit excellent ability for HB manipulation, self-adsorption, Zn^{2+} ion regulation and robust SEI formation. The Zn||Zn symmetrical cells display exceptional cycling stability for over 1800 h at 1 mA cm^{-2} and 1 mA h cm^{-2}. Moreover, a cumulative capacity of over 3700 mA h cm^{-2} can be achieved even at 56.9% ZUR and 10 mA cm^{-2}. The highly stable large-area pouch cell (9 cm^2) and high-capacity Zn||NVO battery (419.1 mA h g^{-1} at 0.2 A g^{-1}) make this sustainable $[CellMim]^+$ show broad application potential in advanced energy storage systems. This study expands a new research strategy for the conversion of inert cellulose resources and promotes the wide application of environmentally friendly bio-based polymer materials in advanced energy storage technologies.

Data availability

The data supporting this article have been included as part of the ESI.†

Author contributions

Kui Chen: methodology, investigation, writing – original draft, writing – review & editing. Yongzhen Xu: data curation, visualization. Hebang Li: data curation, visualization. Yue Li: visualization. Lihua Zhang: formal analysis, visualization. Yuanlong Guo: formal analysis. Qinqin Xu: conceptualization, formal analysis. Yunqi Li: software. Haibo Xie: conceptualization, funding acquisition, methodology, supervision, writing – review & editing.

Conflicts of interest

The authors declare no conflict of interest.

Acknowledgements

This work was supported by the National Natural Science Foundation of China (22275041, 21574030, and 21774028), Science and Technology Department of Guizhou Province (Natural Science Key Fund ZK [2021]023), Guizhou Province Basic Research Program (Z2024021), Qiankehe-Platform JSZX(2025)004, and Qiankehe-Central Government Guided Local Development Funds (2025)032. We thank the Big Data Center for Materials at Guizhou University for computational support. The authors would like to thank Shiyanjia Lab (**https://www.shiyanjia.com**) for transmission electron microscopy (TEM) analysis. The authors would like to thank SCI-GO (**https://www.sci-go.com**) for adsorption energy calculation.

References

1 J. Wei, P. Zhang, J. Sun, Y. Liu, F. Li, H. Xu, R. Ye, Z. Tie, L. Sun and Z. Jin, *Chem. Soc. Rev.*, 2024, **53**, 10335–10369.
2 R. Zhang, W. K. Pang, J. P. Vongsvivut, J. A. Yuwono, G. Li, Y. Lyu, Y. Fan, Y. Zhao, S. Zhang, J. Mao, Q. Cai, S. Liu and Z. Guo, *Energy Environ. Sci.*, 2024, **17**, 4569–4581.
3 F. Luo, S. Yang, Q. Wu, Y. Li, J. Zhang, Y. Zhang, J. Huang, H. Xie and Y. Chen, *Energy Environ. Sci.*, 2024, **17**, 8570–8581.
4 Y. Dai, R. Lu, C. Zhang, J. Li, Y. Yuan, Y. Mao, C. Ye, Z. Cai, J. Zhu, J. Li, R. Yu, L. Cui, S. Zhao, Q. An, G. He, G. I. N. Waterhouse, P. R. Shearing, Y. Ren, J. Lu, K. Amine, Z. Wang and L. Mai, *Nat. Catal.*, 2024, **7**, 776–784.
5 C. Li, A. Shyamsunder, A. G. Hoane, D. M. Long, C. Y. Kwok, P. G. Kotula, K. R. Zavadil, A. A. Gewirth and L. F. Nazar, *Joule*, 2022, **6**, 1103–1120.
6 Q. Wu, J. Huang, J. Zhang, S. Yang, Y. Li, F. Luo, Y. You, Y. Li, H. Xie and Y. Chen, *Angew. Chem., Int. Ed.*, 2024, **63**, e202319051.
7 S. Yang, Q. Wu, Y. Li, F. Luo, J. Zhang, K. Chen, Y. You, J. Huang, H. Xie and Y. Chen, *Angew. Chem., Int. Ed.*, 2024, **63**, e202409160.
8 Y. Liu, X. Lu, F. Lai, T. Liu, P. R. Shearing, I. P. Parkin, G. He and D. J. L. Brett, *Joule*, 2021, **5**, 2845–2903.
9 Z. Zhang, P. Wang, C. Wei, J. Feng, S. Xiong and B. Xi, *Angew. Chem., Int. Ed.*, 2024, **63**, e202402069.
10 S. Chen, D. Ji, Q. Chen, J. Ma, S. Hou and J. Zhang, *Nat. Commun.*, 2023, **14**, 3526.
11 X. Yang, Z. Dong, G. Weng, Y. Su, J. Huang, H. Chai, Y. Zhang, K. Wu, J.-B. Baek, J. Sun, D. Chao, H. Liu, S. Dou and C. Wu, *Adv. Energy Mater.*, 2024, **14**, 2401293.
12 B. Liu, C. Wei, Z. Zhu, Y. Fang, Z. Bian, X. Lei, Y. Zhou, C. Tang, Y. Qian and G. Wang, *Angew. Chem., Int. Ed.*, 2022, **61**, e202212780.
13 S. Wang, S. Wang, Z. Wei, Y. Wang, D. Zhang, Z. Chen and C. Zhi, *Nat. Commun.*, 2025, **16**, 1800.
14 X. Guo, Z. Zhang, J. Li, N. Luo, G.-L. Chai, T. S. Miller, F. Lai, P. Shearing, D. J. L. Brett, D. Han, Z. Weng, G. He and I. P. Parkin, *ACS Energy Lett.*, 2021, **6**, 395–403.
15 F. Wan, L. Zhang, X. Dai, X. Wang, Z. Niu and J. Chen, *Nat. Commun.*, 2018, **9**, 1656.
16 G. Guo, C. Ji, J. Lin, T. Wu, Y. Luo, C. Sun, M. Li, H. Mi, L. Sun and H. J. Seifert, *Angew. Chem., Int. Ed.*, 2024, **63**, e202407417.
17 Y. Meng, M. Wang, J. Wang, X. Huang, X. Zhou, M. Sajid, Z. X. N. A. Khan, Y. Wang, R. Luo, Z. Zhu, Z. Zhang, Z. Li and W. Chen, *Nat. Commun.*, 2024, **15**, 8431.
18 X. Wu, Y. Dai, N. W. Li, X. C. Chen and L. Yu, *eScience*, 2024, **4**, 100173.
19 X. Liao, S. Chen, J. Chen, Y. Li, W. Wang, T. Lu, Z. Chen, L. Cao, Y. Wang, R. Huang, X. Sun, R. Lv and H. Wang, *Proc. Natl. Acad. Sci. U.S.A.*, 2024, **121**, e2317796121.

20 P. Xu, M. Xu, J. Zhang, J. Zou, Y. Shi, D. Luo, D. Wang, H. Dou and Z. Chen, *Angew. Chem., Int. Ed.*, 2024, **63**, e202407909.
21 M. Peng, X. Tang, K. Xiao, T. Hu, K. Yuan and Y. Chen, *Angew. Chem., Int. Ed.*, 2023, **62**, e202302701.
22 W. Xu, J. Li, X. Liao, L. Zhang, X. Zhang, C. Liu, K. Amine, K. Zhao and J. Lu, *J. Am. Chem. Soc.*, 2023, **145**, 22456–22465.
23 D. Wang, R. Li, J. Dong, Z. Bai, N. Wang, S. X. Dou and J. Yang, *Angew. Chem., Int. Ed.*, 2024, **64**, e202414117.
24 H. Wang, W. Ye, B. Yin, K. Wang, M. S. Riaz, B. B. Xie, Y. Zhong and Y. Hu, *Angew. Chem., Int. Ed.*, 2023, **62**, e202218872.
25 P. Sun, L. Ma, W. Zhou, M. Qiu, Z. Wang, D. Chao and W. Ma, *Angew. Chem., Int. Ed.*, 2021, **60**, 18247–18255.
26 H. Li, Y. Ren, Y. Zhu, J. Tian, X. Sun, C. Sheng, P. He, S. Guo and H. Zhou, *Angew. Chem., Int. Ed.*, 2023, **62**, e202310143.
27 K. Chen, Y. Chen, Y. Xu, M. Xu, Y. Li, S. Yang, Q. Wu, Q. Xu, H. Xie and J. Huang, *Energy Storage Mater.*, 2024, **71**, 103597.
28 M. Pei, X. Peng, Y. Shen, Y. Yang, Y. Guo, Q. Zheng, H. Xie and H. Sun, *Green Chem.*, 2020, **22**, 707–717.
29 Y. Yang, Y. Guo, C. Gao, M. North, J. Yuan, H. Xie and Q. Zheng, *ACS Sustainable Chem. Eng.*, 2023, **11**, 2634–2646.
30 K. Chen, J. Huang, J. Yuan, S. Qin, P. Huang, C. Wan, Y. You, Y. Guo, Q. Xu and H. Xie, *Energy Storage Mater.*, 2023, **63**, 102963.
31 Y. Chen, Y. Wang, J. Wan and Y. Ma, *Cellulose*, 2009, **17**, 329–338.
32 L. Liu, X.-Y. Wang, Z. Hu, X. Wang, Q. Zheng, C. Han, J. Xu, X. Xu, H.-K. Liu, S.-X. Dou and W. Li, *Angew. Chem., Int. Ed.*, 2024, **63**, e202405209.
33 X. Yu, M. Chen, Z. Li, X. Tan, H. Zhang, J. Wang, Y. Tang, J. Xu, W. Yin, Y. Yang, D. Chao, F. Wang, Y. Zou, G. Feng, Y. Qiao, H. Zhou and S.-G. Sun, *J. Am. Chem. Soc.*, 2024, **146**, 17103–17113.
34 D. Feng, Y. Jiao and P. Wu, *Angew. Chem., Int. Ed.*, 2023, **62**, e202314456.
35 J. Cao, Y. Sun, D. Zhang, D. Luo, L. Zhang, R. Chanajaree, J. Qin, X. Yang and J. Lu, *Adv. Energy Mater.*, 2024, **14**, 2302770.
36 X. Wang, L. Liu, Z. Hu, C. Han, X. Xu, S. Dou and W. Li, *Chem. Sci.*, 2024, **15**, 17348–17361.
37 W. Guo, L. Xu, Y. Su, L. Zhao, Y. Ding, Y. Zou, G. Zheng, T. Cheng and J. Sun, *Angew. Chem., Int. Ed.*, 2024, **64**, e202417125.
38 K. Ouyang, F. Li, D. Ma, Y. Wang, S. Shen, M. Yang, J. Qiu, W. Wen, N. Zhao, H. Mi and P. Zhang, *ACS Energy Lett.*, 2023, **8**, 5229–5239.
39 Y. Pan, Z. Zuo, Y. Jiao and P. Wu, *Adv. Mater.*, 2024, **36**, 2314144.
40 J. Luo, L. Xu, Y. Zhou, T. Yan, Y. Shao, D. Yang, L. Zhang, Z. Xia, T. Wang, L. Zhang, T. Cheng and Y. Shao, *Angew. Chem., Int. Ed.*, 2023, **62**, e202302302.
41 J. Poisson and K. Zhang, *Acc. Mater. Res.*, 2024, **5**, 920–932.
42 K. Wang, Q. Li, G. Zhang, S. Li, T. Qiu, X. X. Liu and X. Sun, *Chem. Sci.*, 2023, **15**, 230–237.
43 Z. Yi, G. Chen, F. Hou, L. Wang and J. Liang, *Adv. Energy Mater.*, 2020, **11**, 2003065.
44 B. D. Adams, J. Zheng, X. Ren, W. Xu and J.-G. Zhang, *Adv. Energy Mater.*, 2018, **8**, 1702097.
45 J. Luo, L. Xu, Y. Yang, S. Huang, Y. Zhou, Y. Shao, T. Wang, J. Tian, S. Guo, J. Zhao, X. Zhao, T. Cheng, Y. Shao and J. Zhang, *Nat. Commun.*, 2024, **15**, 6471.
46 H. Gan, H. Li, M. Xu, C. Han and H.-M. Cheng, *Joule*, 2024, **8**, 1–18.
47 Q. Wu, J. Zhang, S. Yang, F. Luo, Z. Yan, X. Liu, H. Xie, J. Huang and Y. Chen, *Angew. Chem., Int. Ed.*, 2024, **64**, e202418524.
48 B. Liu, L. Yu, Q. Xiao, S. Zhang, G. Li, K. Ren, Y. Zhu, C. Wang and Q. Wang, *Chem. Sci.*, 2024, **15**, 16118.
49 K. Wang, S. Li, X. Chen, J. Shen, H. Zhao and Y. Bai, *ACS Nano*, 2024, **18**, 7311–7323.
50 C. Li, S. Jin, L. A. Archer and L. F. Nazar, *Joule*, 2022, **6**, 1733–1738.